OPEN ACCESS

KING'S College LONDON

King's Research Portal

Document Version
Peer reviewed version

Link to publication record in King's Research Portal

Citation for published version (APA):
Padormo, F., Cawley, P., Dillon, L., Hughes, E., Almalbis, J., Robinson, J., Maggioni, A., De la Fuente Botella, M., Cromb, D., Price, A., Arlinghaus, L., Pitts, J., Luo, T., Zhang, D., Deoni, S. C. L., Williams, S., Malik, S., O'Muircheartaigh, J., Counsell, S., ... Hajnal, J. (Accepted/In press). In-Vivo T1 Mapping of Neonatal Brain Tissue at 64mT. *Magnetic resonance in medicine*.

Citing this paper
Please note that where the full-text provided on King's Research Portal is the Author Accepted Manuscript or Post-Print version this may differ from the final Published version. If citing, it is advised that you check and use the publisher's definitive version for pagination, volume/issue, and date of publication details. And where the final published version is provided on the Research Portal, if citing you are again advised to check the publisher's website for any subsequent corrections.

General rights
Copyright and moral rights for the publications made accessible in the Research Portal are retained by the authors and/or other copyright owners and it is a condition of accessing publications that users recognize and abide by the legal requirements associated with these rights.

•Users may download and print one copy of any publication from the Research Portal for the purpose of private study or research.
•You may not further distribute the material or use it for any profit-making activity or commercial gain
•You may freely distribute the URL identifying the publication in the Research Portal

Take down policy
If you believe that this document breaches copyright please contact librarypure@kcl.ac.uk providing details, and we will remove access to the work immediately and investigate your claim.

Download date: 08. Oct. 2023

In-Vivo T_1 Mapping of Neonatal Brain Tissue at 64mT

Francesco Padormo[1,2,5*], Paul Cawley[1,3,4*], Louise Dillon[1], Emer Hughes[1], Jennifer Almalbis[1,4], Joanna Robinson[1,4], Alessandra Maggioni[1,4], Miguel De La Fuente Botella[1,4], Dan Cromb[1,4], Anthony Price[1], Lori Arlinghaus[5], John Pitts[5], Tianrui Luo[5], Dingtian Zhang[5], Sean C. L. Deoni[6,7,8], Steve Williams[3,9], Shaihan Malik[1], Jonathan O'Muircheartaigh[1,3,10], Serena J. Counsell[1], Mary Rutherford[1,3], Tomoki Arichi[1,3,11,12], A. David Edwards[1,3,4], Joseph V. Hajnal[1**]

1 - Centre for the Developing Brain, School of Imaging Sciences and Biomedical Engineering, King's College London, London, UK

2 - Medical Physics, Guy's & St Thomas' NHS Foundation Trust, London, UK.

3 – MRC Centre for Neurodevelopmental Disorders, King's College London, London, UK.

4 - Department of Neonatology, Guy's and St Thomas' NHS Foundation Trust, London, UK.

5 - Hyperfine, Inc., Connecticut, USA.

6 - Advanced Baby Imaging Lab, Rhode Island Hospital, Warren Alpert Medical School at Brown University, Providence, RI, USA.

7 - Department of Diagnostic Radiology, Warren Alpert Medical School at Brown University, Providence, RI, USA.

8 - Department of Pediatrics, Warren Alpert Medical School at Brown University, Providence, RI, USA.

9 - Centre for Neuroimaging Sciences, King's College London, UK

10 – Department of Forensic and Neurodevelopmental Science, Institute of Psychiatry, Psychology and Neuroscience, King's College London, London, UK

11 - Department of Bioengineering, Imperial College London, UK

12 - Paediatric Neurosciences, Evelina London Children's Hospital, Guys' and St Thomas' NHS Foundation Trust, London, UK

* Authors contributed equally to this work

** Corresponding author: jo.hajnal@kcl.ac.uk

Abstract

Purpose:

Ultra-low field (ULF) point-of-care MRI systems allow image acquisition without interrupting medical provision, with neonatal clinical care being an important potential application. The ability to measure neonatal brain tissue T_1 is a key enabling technology for subsequent structural image contrast optimisation, as well as being a potential biomarker for brain development. Here we describe an optimised strategy for neonatal T_1 mapping at ULF.

Methods:

Examinations were performed on a 64mT portable MRI system. A phantom validation experiment was performed, and total of thirty-three in-vivo exams were acquired from twenty-eight neonates with postmenstrual age ranging 31^{+4} to 49^{+0} weeks. Multiple inversion-recovery turbo spin echo sequences were acquired with differing inversion and repetition times. An analysis pipeline incorporating inter-sequence motion correction generated proton density and T_1 maps. Regions of interest were placed in the cerebral deep grey matter, frontal white matter and cerebellum. Weighted linear regression was used to predict T_1 as a function of postmenstrual age.

Results:

Reduction of T_1 with postmenstrual age is observed in all measured brain tissue; the change in T_1 per week and 95% confidence intervals is given by dT_1=-21ms/week [-25, -16] (cerebellum), dT_1=-14ms/week [-18, -10] (deep grey matter), and dT_1=-35ms/week [-45, -25] (white matter).

Conclusion:

Neonatal T_1 values at ULF are shorter than those previously described at standard clinical field strengths, but longer than those of adults at ULF. T_1 reduces with postmenstrual age and is thus a candidate biomarker for perinatal brain development.

Keywords: Ultra Low Field MRI, Relaxometry, Neonatal, White Matter, Grey Matter

Word Count: 3,544

Introduction

Recent years have seen increased popularity of MRI systems utilising magnetic field strengths far below those of traditional clinical systems with superconducting magnets. These systems have been engineered to optimise alternative design criteria (such as increased portability and lowered cost) in contrast to high field systems, which generally aim to maximise image quality. Crucially, these low-field systems can also have reduced infrastructure needs, promising to expand the use of MRI beyond radiology departments in high-income countries.

Ultra-low field (ULF) point-of-care (POC) MRI systems (1–5) are a category of device designed to allow image acquisition without interrupting a patient's medical provision. Neonatal clinical care is an important potential application, as portable systems would allow imaging on Neonatal Intensive Care Units in both high and lower-resourced settings and where rapid diagnostic information could have large implications for clinical decision making. Key examples include neonates suffering from neurological pathologies such as hypoxic ischaemic injury, hydrocephalus, stroke, as well as other conditions elsewhere in the body.

Although neonatal brain MRI has been performed at a variety of field strengths (6–10), there is limited work in this cohort at ULF. Whilst ULF adult imaging has been successfully demonstrated (11), initial local experience demonstrates that sequences and acquisition parameters optimized for adults do not necessarily provide optimal image contrast in younger cohorts. This phenomenon is likely due to marked relaxation rate differences between adult and neonatal brain tissues, demonstrated at both high field in vivo (12–17) and at ULF in ex-vivo tissue samples (18).

The ability to measure neonatal brain tissue longitudinal relaxation time (T_1) is a key enabling technology for further ULF neonatal imaging. It will allow image contrast optimisation for structural imaging, as well as having the potential to be a biomarker for neonatal brain development. However, there has been no in-vivo ULF neonatal T_1 mapping to date, motivating this work utilising a 64mT portable MRI system. Here we describe an optimised strategy for T_1 mapping using an inversion recovery turbo spin echo (TSE) sequence and report values in 28 neonates.

Methods

We designed a combined acquisition and analysis strategy to allow T_1 mapping in the presence of participant motion, typical in neonates and infants. Multiple T_1-weighted volumes are first acquired, with each acquisition designed to have short duration to minimise the chance of intra-volume motion corruption.

The reconstruction pipeline then takes an iterative two-step approach. First, data fitting is performed without any correction for inter-sequence motion. The resulting proton density (M_0) and T_1 maps are then used to synthesise new images with the same T_1-weighting as the acquired data, to which the original images are registered. These registered images are then used for data fitting, with this process repeated for a fixed number of iterations.

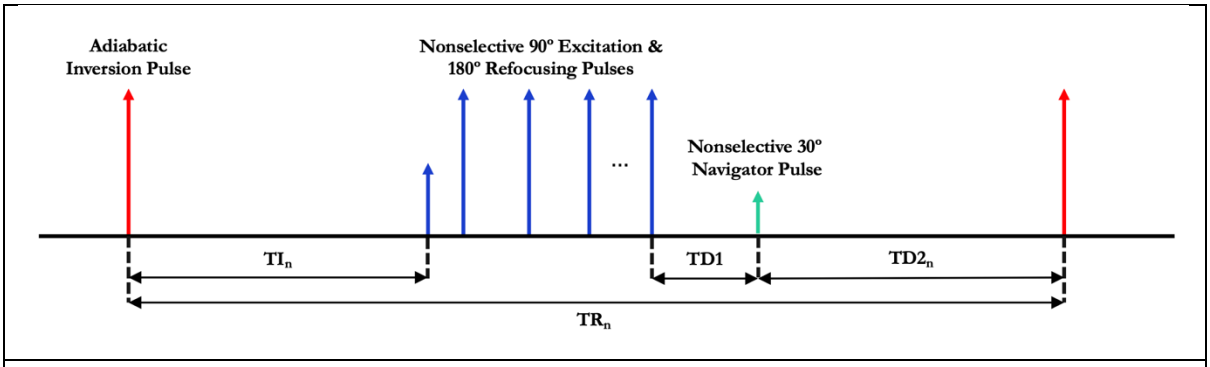

Figure 1 - Pulse sequence diagram of inversion recovery 3D turbo spin echo. The sequence is comprised of an adiabatic inversion pulse, a turbo spin echo read-out train, and a centre frequency navigator.

Acquisition

Two phantom experiments were performed to validate the acquisition and analysis pipeline used for our in-vivo neonatal studies. A contrast phantom comprised of six 50mL falcon tubes containing distilled water and $MnCl_2$ at concentrations of 0, 0.01, 0.05, 0.1, 0.15 and 0.2mM, placed in a custom-built holder so that the long axes of the vials were aligned with the main magnetic field. The second, a homogeneity phantom, was a spherical flask of diameter of 144mm containing a solution of saline and gadolinium doped to achieve a T_1 in the range of neonatal white matter at 64mT.

A total of thirty-three exams were acquired from twenty-eight neonates (mean gestation at birth: 36^{+3} weeks$^{+\text{days}}$, range: [27^{+0}, 40^{+4}], mean age at first scan: 13 days, range: [1, 94], mean

postmenstrual age at scan: 39^{+2} weeks^{+days}, range: [31^{+4}, 49^{+0}]), as part of two NHS UK Research Ethics Committee approved studies (12/LO/1247, 19/LO/1384). Recruitment to these studies included healthy controls and clinically referred neonates. Infants referred for clinical scans were eligible for Chloral Hydrate sedation. All medical support requirements, such as ventilation, intra-venous infusions and/or thermoregulation were continued throughout scanning, alongside continuous oxygen saturation and heart rate monitoring. Subjects were swaddled and immobilised using a vacuum-evacuated bag containing polystyrene beads and placed in a neonatal imaging cradle designed to position the neonate's head at the magnet isocentre. Imaging utilised a 64mT Swoop® portable MRI system (Hyperfine, Inc., Guilford, CT), utilising the built-in radiofrequency interference rejection method (19) and single channel transmit/eight channel receive coil.

The scanning protocol comprised a pre-scan calibration, localiser, and several acquisitions of the Hyperfine product inversion-recovery 3D turbo spin echo (TSE) acquisition (Figure 1), each modified using the sequence development interface to have differing repetition and inversion times (TR_n, TI_n, with the subscript indexing the multiple acquisitions). The base sequence contains an adiabatic inversion pulse, a T_1 recovery period (TI_n), a non-selective TSE read-out of N_{TF} echoes utilising low-high phase-encode ordering, a delay period TD1 between the read-out and a centre-frequency navigator echo generated by a non-selective excitation of flip angle θ_{nav}, followed by a recovery time $TD2_n$. The signal S_n at the first echo for a given choice (TR_n, TI_n) is given by 1; note that the contribution from non-zero TE is subsumed into the M_0 term.

1	$S_n(M_0, T_1; TR_n, TI_n) = M_0\left(1 - e^{-TI_n/T_1}\right) - M_0\left(\left(1 - e^{-TD1/T_1}\right)\cos(\theta_{nav})\, e^{-TD2_n/T_1} + \left(1 - e^{-TD2_n/T_1}\right)\right) e^{-TI_n/T_1}$

The following base sequence parameters were used for all acquisitions: field of view = 180 x 220 x 180mm (RL x AP x FH), resolution = 2.8 x 2.8 x 2.8mm, turbo factor (N_{TF}) = 48, echo spacing (τ) = 4.62ms, BW = 64kHz, excitation flip angle = 90°, refocusing flip angle = 180°, TE = 4.62ms, θ_{nav} = 30°, TD1 = 239ms, and $TD2_n$ = TR_n-TI_n-$N_{TF}\tau$-TD1. Preliminary experiments confirmed insensitivity to transmitter voltage miscalibration.

The comprehensive mapping protocol is given by row 0 in Table 1. This was used exclusively for the phantom acquisitions, with the protocol acquired at lower resolution (5 x 5 x 5mm) for the homogeneity phantom to increase measurement signal-to-noise ratio. Additionally, the homogeneity phantom experiment included the acquisition of a B_1+ map using Actual Flip-angle

Imaging (AFI) (20) with the following sequence parameters: TR1 = 20ms, TR2 = 100ms, TE = 2.56ms, flip angle = 90°, BW = 20kHz, field of view = 210 x 210 x 210mm, resolution = 5 x 5 x 5mm.

Other variants were also utilised (rows 1-7), reflecting the need to limit total acquisition time for neonatal scanning as per study protocol (protocol 1), abbreviated scanning sessions due to other clinical priorities and neonates awaking from sleep (protocols 2-4), or initial trial versions of the protocol before modification to improve performance for longer relaxation times (protocols 5-7). All data is included to maximise the number of subjects included in the study. Additionally, note that the listed inversion times are those entered on the system's user-interface; the physical inversion times are 5.75ms longer. Sequences utilising TR = 1500ms had a total duration of 3m32s; sequences utilising TR = 3000ms had a total duration of 7m04s.

#	Acquisition Protocol	Number of In-Vivo Acquisitions
0	TI = [100, 200, 300, 400, 500, 600, 700, 800, 1010, 900] TR = [1500, 1500, 1500, 1500, 1500, 1500, 1500, 1500, 1500, 3000]	0
1	TI = [100, 300, 400, 500, 600, 800, 1010, 900] TR = [1500, 1500, 1500, 1500, 1500, 1500, 1500, 3000]	12
2	TI = [100, 300, 500, 600, 800, 1010, 900] TR = [1500, 1500, 1500, 1500, 1500, 1500, 3000]	8
3	TI = [100, 300, 400, 500, 600, 800, 1010] TR = [1500, 1500, 1500, 1500, 1500, 1500, 1500]	1
4	TI = [400, 500, 600, 800, 1010, 900] TR = [1500, 1500, 1500, 1500, 1500, 3000]	1
5	TI = [100, 200, 300, 400, 500, 600, 700, 800, 1010] TR = [1500, 1500, 1500, 1500, 1500, 1500, 1500, 1500, 1500]	2
6	TI = [100, 200, 300, 400, 500, 600, 700, 800] TR = [1500, 1500, 1500, 1500, 1500, 1500, 1500, 1500]	4
7	TI = [100, 200, 300, 400, 500, 600] TR = [1500, 1500, 1500, 1500, 1500, 1500]	5

Table I – Imaging parameters of the protocols used within presented study, and number of acquisitions each protocol was utilised.

Reconstruction – Data Fitting

Magnitude images were exported from the scanner in DICOM format, with the following steps performed for each participant. An initial brain and scalp mask was generated utilising FSL BET (21) with fractional threshold set to 0.1. This mask was manually edited to exclude the face, mouth, and all anatomy inferior to the brain to allow utilisation of rigid-body registration in

subsequent processing steps. Phantom images were masked by image thresholding using Matlab (The Mathworks, Inc., Natick, MA).

Fitting was performed using Matlab. The low signal-to-noise ratio of ULF-MRI and the magnitude-only image intensities available via data export results in a Rician distribution of image noise (22). It is appropriate to use statistical parameter estimation methods designed for the statistical noise distribution present in the data. In this case, the optimisation problem stated as Equation 2 is obtained by maximising the log-likelihood function given Rician-distributed noise (23). Herein Φ is the cost function, n is an index over the N acquisitions, σ is the standard deviation of the underlying Gaussian-distributed noise, I_0 is the zeroeth order modified Bessel function, and d_n is the measured signal of the n^{th} acquisition. An estimate of σ is obtained by finding the mean signal $\bar{\sigma}_{Rician}$ in a region of interest (ROI), manually placed in a region avoiding signal and artifacts, and using the relation $\sigma = \bar{\sigma}_{Rician}/\sqrt{\pi/2}$.

2	$$\min_{M_0,T_1} \Phi = \sum_{n=1}^{N} \frac{\lvert S_n(TR_n, TI_n, M_0, T_1)\rvert^2}{2\sigma^2} - \ln\left(I_0\left(\frac{d_n \lvert S_n(TR_n, TI_n, M_0, T_1)\rvert}{\sigma^2}\right)\right)$$

The cost function was minimised for each voxel in the mask using a two-step procedure. A coarse search was first performed (160,000 M_0 & T_1 combinations; range [0, 1000] and [50ms, 4000ms], respectively) to obtain an estimate of the solution. This was used as the initial point when minimising the cost function using the fmincon routine, with the solutions constrained to lie in the ranges utilised in the coarse search. This process yielded M_0 and T_1 maps.

Reconstruction – Motion Compensation

These initial M_0 and T_1 maps were then used in conjunction with Equation 1 to generate synthetic images for each acquired sequence. These synthetic images were used as registration targets to which the acquired images were registered. The registration is performed with FSL FLIRT (24,25) using a rigid body transformation and sinc interpolation, with the previously defined mask used to exclude areas that may have undergone non-rigid motion. These registered acquired images were then again used for data fitting. The whole process was repeated until convergence, with local experience indicating that three iterations were sufficient.

Phantom Data Analysis

Both phantom datasets (acquired as per protocol 0 in Table I) were reconstructed with the pipeline outlined above. However, the contrast phantom data was reconstructed eight times in total, each using the appropriate set of source images as prescribed by protocols 0-7 in Table I. The T_1 of all voxels within each vial were extracted and the mean and standard deviation calculated. In order to assess the validity of the acquisition, each protocol and the reconstruction pipeline, a linear weighted least-squares fit was performed for each protocol and results plotted against concentration (c) of $MnCl_2$ to confirm consistency with the known relationships given by equation 3, where $T_1(c=0)$ is the unknown relaxation time of the distilled water at 64mT and R is the concentration of added salt in mM. The r^2 for each fit was used to evaluate data to model consistency.

3	$1/T_1(c) = 1/T_1(c = 0) + Rc$

In-Vivo Region of Interest Analysis

The final set of synthesised in-vivo neonatal images were visually examined by a single reader (FP) to place ROIs in the deep grey matter (putamen/caudate), frontal white matter and cerebellum. For each anatomical location, ROIs of size 2x2x2 voxels were placed on both the left and right of the brain. The mean and standard deviation T_1 values were calculated for each anatomical location to obtain per subject values. A group analysis was performed by calculating a weighted linear regression to predict T_1 as a function of postmenstrual age; the weights were taken as the inverse square of the standard deviations.

Results

Figure 2 shows the results of the contrast phantom validation experiment. Figure 2A shows the measured T_1 versus concentration for protocol 0, with datapoints and error bars indicating the mean and standard deviations of all voxels within each vial. The dashed black lines indicate the fit to equation 3. The r^2 values of the fits to equation 3 were greater than 0.997 for all protocols, indicating that the pulse sequence, protocols and reconstruction pipeline are valid.

Figure 2B shows the results of reconstructing the contrast phantom data presuming the acquisition protocols outlined in Table I. The vertical axes show the fractional difference between the measured T_1's versus those predicted via the model fit for protocol 0. All but three measurements (protocol 7, 0.01mM; protocols 1 and 2, 0.05mM) are within one standard deviation of the model. Different protocols show different degrees of bias and variance as compared to protocol 0, and differences are seen as a function of T_1.

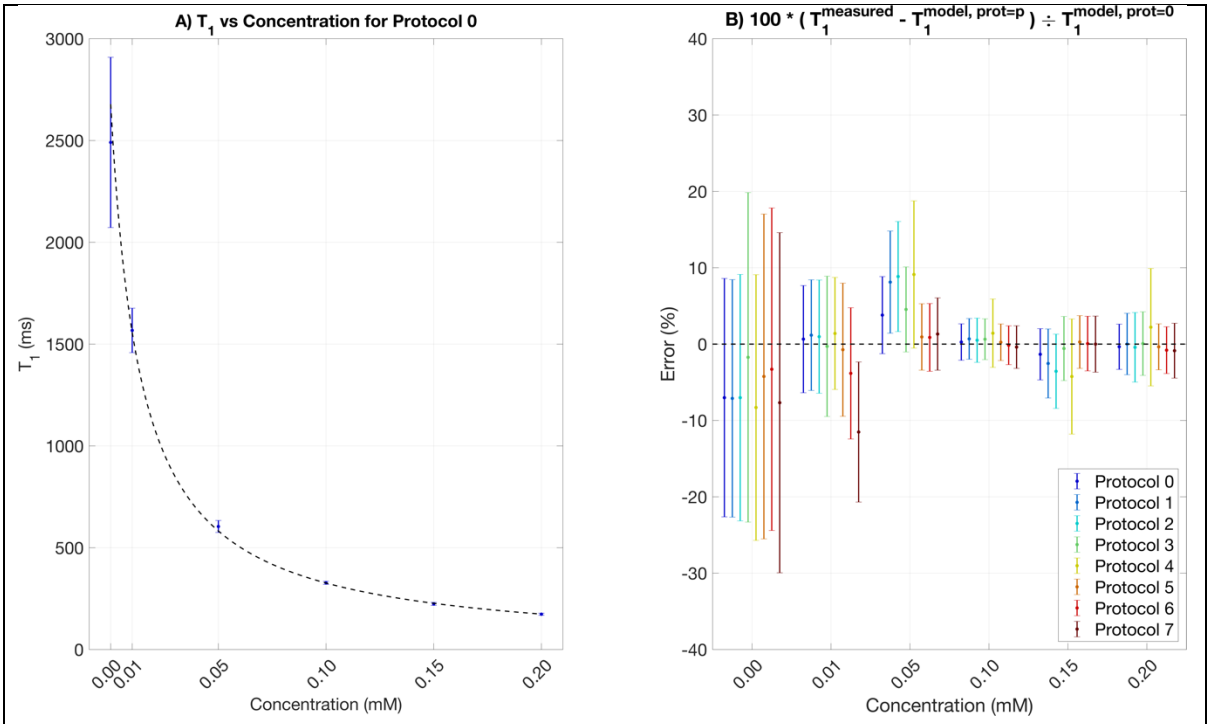

Figure 2 – Results of contrast phantom validation experiment.

Figure 3 shows the result of the homogeneity phantom experiment. Figure 3A show the B_1+ of three orthogonal slices through the phantom. Whilst there is little appreciable inhomogeneity in the transverse plane (top row), there is a 15-20% variation in the superior-inferior direction. This is shown further by the black line profiles in the second and third rows of Figure 3B. Despite the

B_1+ inhomogeneity present, Figure 3C and D demonstrate this does not introduce spatial variation in the T_1 measurements.

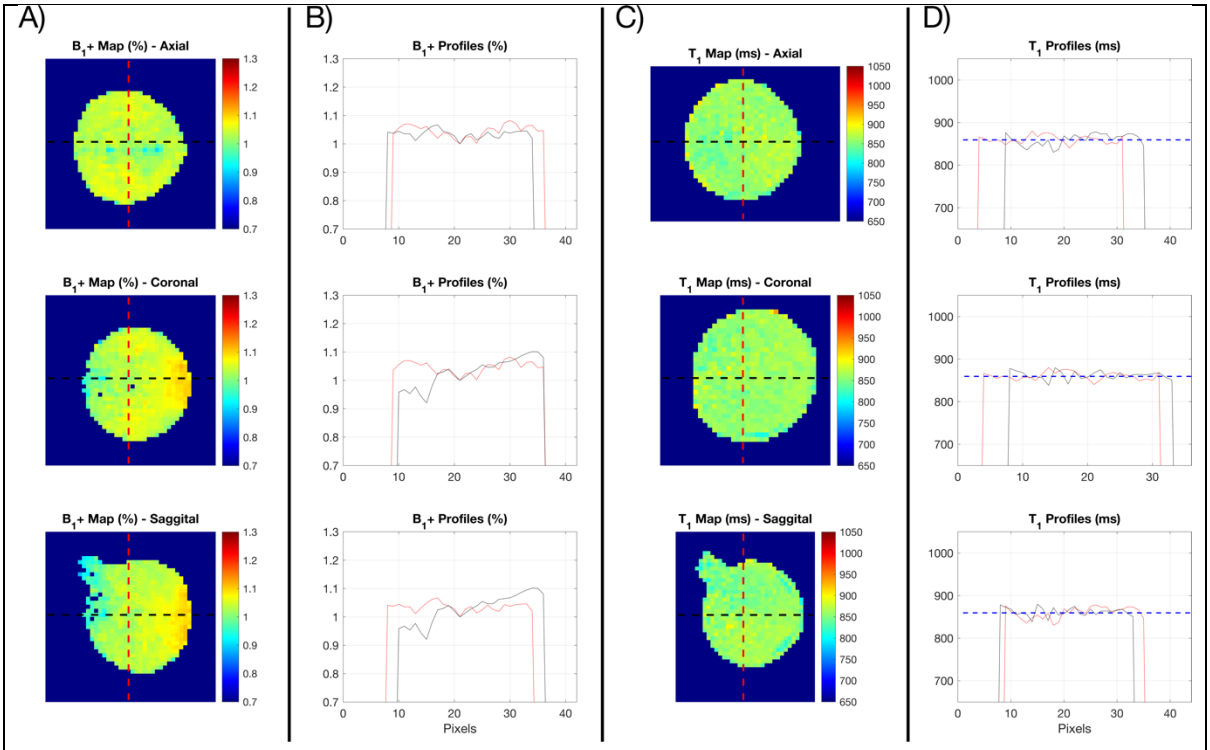

Figure 3 – Results of homogeneity phantom validation experiment.

Supporting Information Videos S1 and S2 show the effect of the inter-sequence motion correction pipeline for three participants with varying degrees of motion. In each case, the top row shows the source data prior to inter-sequence motion correction, and the bottom row shows the source data after three iterations of the proposed reconstruction pipeline. Whilst there is still motion present in the images after correction, motion is only present outside of the brain parenchyma; the brain after correction is static.

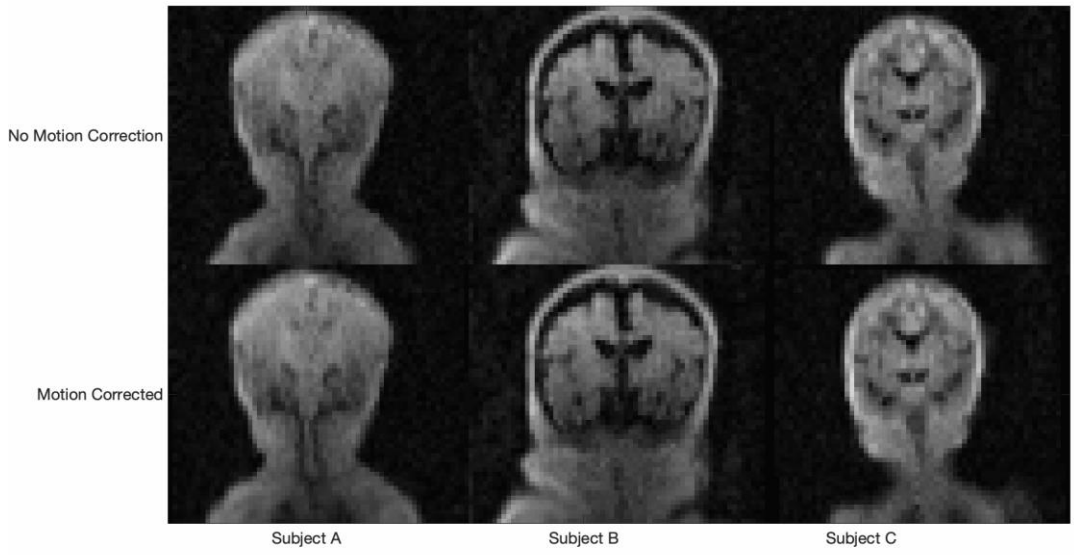

Supporting Information Video S1 – Top row: coronal images prior to motion compensation. Contrast changes across the volume are seen due to varying sequence parameters, and inter-image motion is observed. Bottom row: After inter-volume motion compensation, the brain remains static in the frame. Nonlinear motion is still observed outside of the head, but is not relevant for T_1 mapping in the brain.

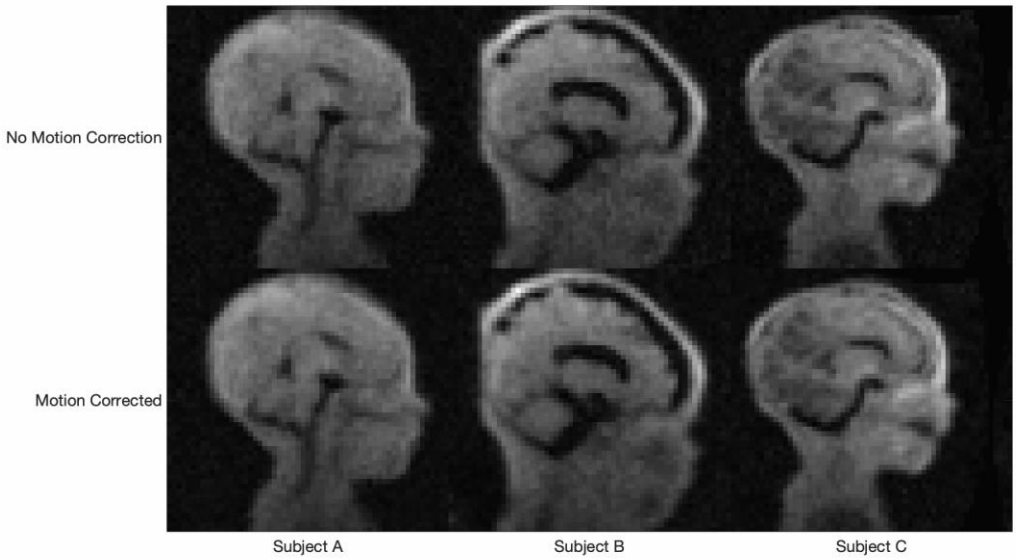

Supporting Information Video S2 – Top row: saggital images prior to motion compensation. Contrast changes across the volume are seen due to varying sequence parameters, and inter-image motion is observed. Bottom row: After inter-volume motion compensation, the brain

remains static in the frame. Nonlinear motion is still observed outside of the head, but is not relevant for T_1 mapping in the brain.

Figure 4 shows example data from one subject (gestation 33^{+2}, post-menstrual age 34^{+0}). Figure 4A shows the three axial slices containing the selected regions of interest for all acquired sequences, with the centre of each ROI in a single hemisphere marked. Figure 4B and Figure 4C show M_0 and T_1 maps for the same slices. Figure 4D-F show the intensity of the centre pixel of each selected ROI (blue points). To allow visual evaluation of the fitting procedure, the measured M_0 and T_1 were used in conjunction with equation 1 to predict the signal as a function of TI assuming TR=1500ms (red line), and for TI=900ms and TR=3000ms (red cross).

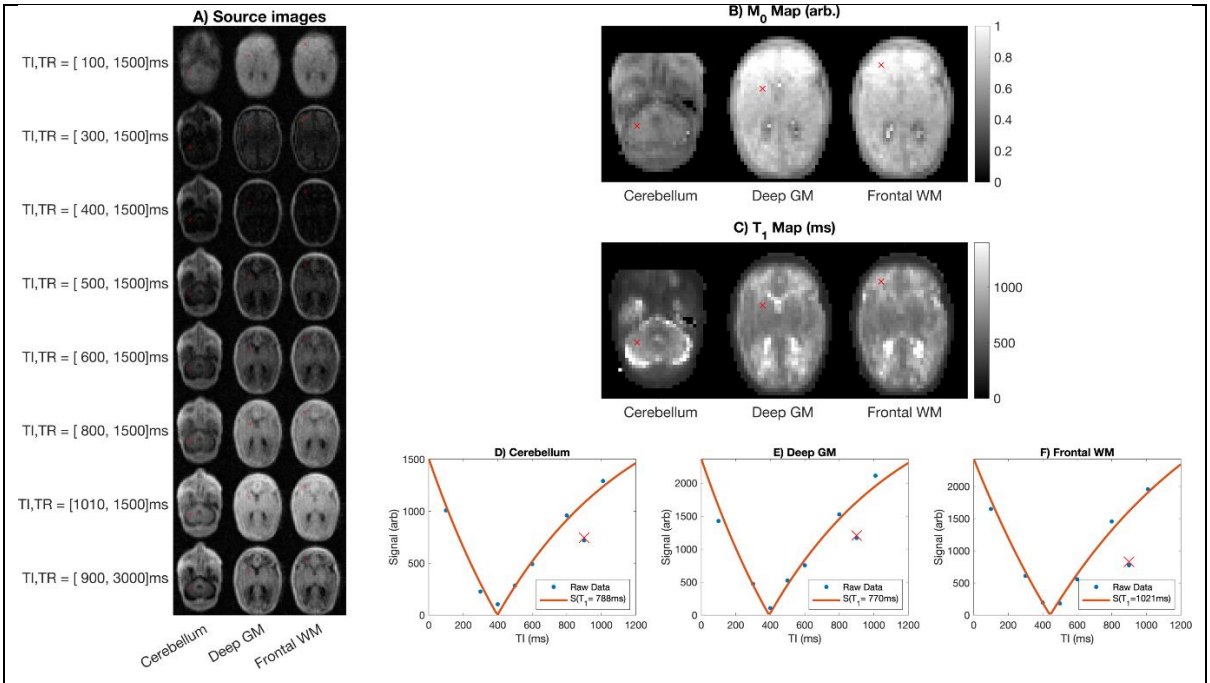

Figure 4 – Three slices from a single neonate (gestation 33^{+2}, post-menstrual age 34^{+0}) A) Source images for each T_1w acquisition; B,C) M_0 and T_1 maps; and D-F) Raw datapoints (blue dots) and predicted signals (red lines/cross) based on measured T_1 and M_0. The blue datapoint/red cross away from the curve corresponds to the TR=3000ms datapoint, and therefore belongs to a separate inversion-recovery curve.

Figure 5 shows the impact of image registration on T_1 map quality. Figure 5A and B show coronal and axial T1 maps for the three iterations of the reconstruction pipeline. Later iterations of the T_1 maps have fewer spurious individual pixels intensities, as for example in the deep grey matter which has a more uniform appearance. Figure 5C and D show root-mean square error

(RMSE, between the input images and the predicted images) maps as a fraction of the average input image pixel intensity across acquisitions at each iteration. The relative RMSE (rRMSE) error reduces for increasing number of iterations.

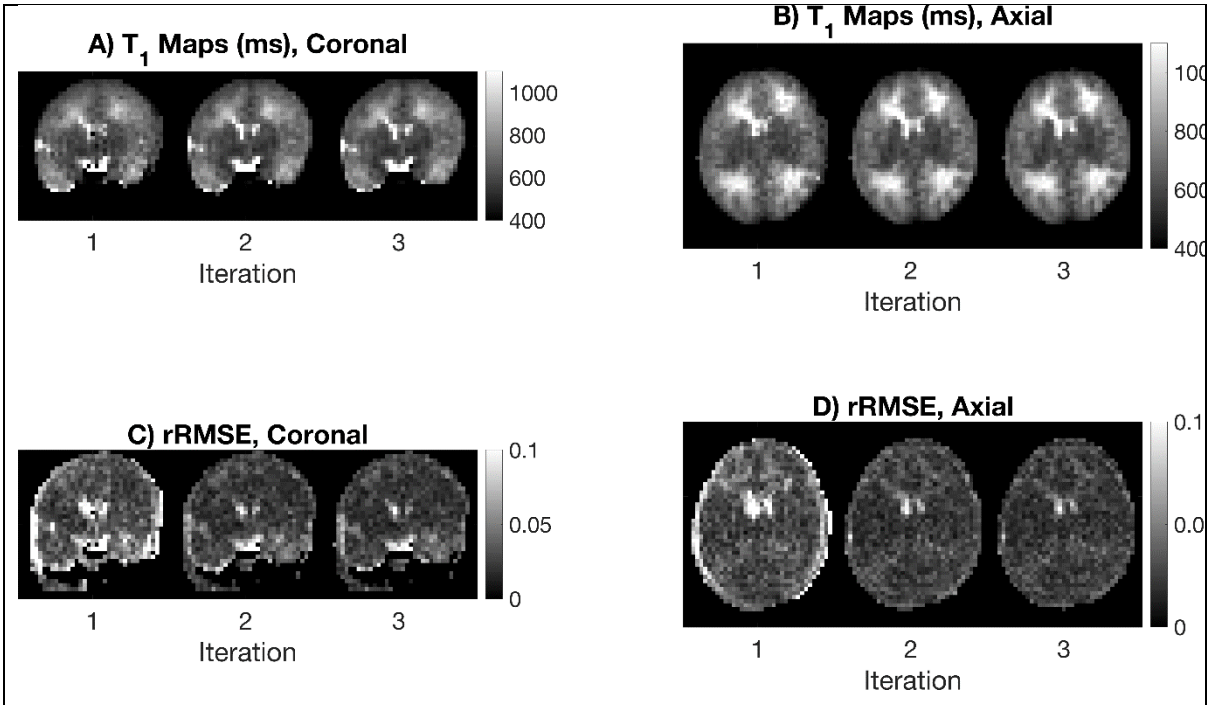

Figure 5 – The effect of motion correction on T_1 maps of a neonate born at 38^{+3} gestation and imaged at 41^{+0} post-menstrual age. Coronal (A) and axial (B) T_1 maps for three iterations of the reconstruction pipeline. Coronal (C) and axial (D) the relative root-mean square error maps between the input images and predicted output images at each iteration.

Figure 6 shows example T_1 maps for eight subjects ordered by postmenstrual age at scan in weeks (31-49 weeks). Maps have isotropic voxel size and demonstrate the ability to differentiate white matter, grey matter and CSF spaces.

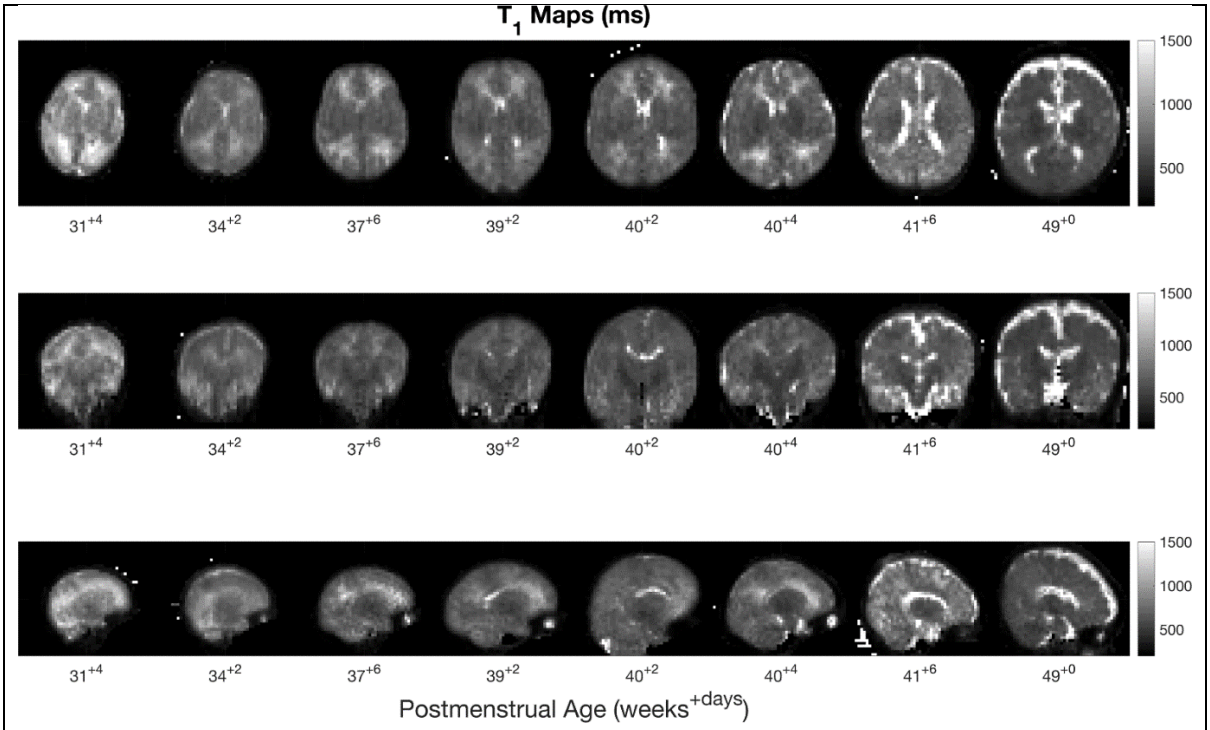

Figure 6 – T_1 maps of eight subjects over the full age range of neonates scanned in this study.

Figure 7 shows the T_1 values plotted against postmenstrual age. Reduction of T_1 with postmenstrual age is observed in all three brain regions, with the change in T_1 per week and 95% confidence intervals given by dT_1=-21ms/week [-25, -16] (cerebellum), dT_1=-14ms/week [-18, -10] (deep grey matter), and dT_1=-35ms/week [-45, -25] (white matter).

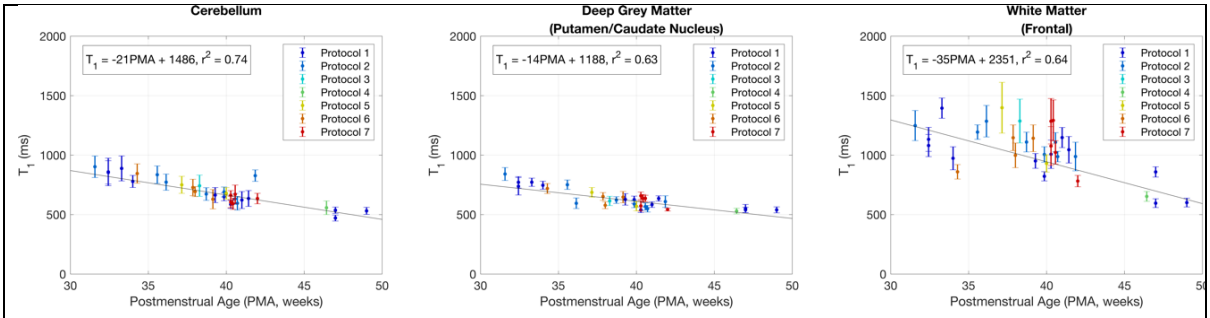

Figure 7 – T_1 versus postmenstrual age. The colour of each datapoint indicates the acquisition protocol from Table I.

Discussion

This study presents first results from an acquisition method and novel reconstruction pipeline to achieve motion compensated T_1 relaxation rate mapping in the neonatal brain at 64mT.

The proposed methodology utilised an inversion-recovery TSE for image acquisition. This sequence was chosen due to its widespread use in prior T_1 mapping publications, including at ultra-low field (26). Whilst individual sequence acquisition times were short (3m32s or 7m04s, depending on TR), the overall protocols ranged from 21mins to 32mins. Though this extended protocol duration is viable for a research study, future work could utilise methods which acquire data in a shorter amount of time, allowing for clinical use where time is more limited (27).

The presented study used a varying protocol across our cohort. This reflected the practicalities of imaging neonates in a neonatal unit where a scan may be terminated early to prioritise other clinical work, as well as intentional modifications to the protocol to improve accuracy for longer relaxation times. Future work will utilise a protocol optimised using the appropriate efficiency metric (28) for the range of T_1s we have observed in neonates, accounting for a desired protocol duration, as well as accounting for the possibility of individual sequence failures due to motion, and the fact any protocol may be truncated due to competing clinical pressures.

The results show that measured neonatal brain T_1 values at ULF are shorter than those at standard clinical field strengths (12–14,29), but longer than those of adults at ULF (26). The results also show that T_1 reduces with postmenstrual age, which is thought to reflect an interplay between maturation and key facets of brain tissue composition including water content and myelination. Whilst this trend is consistent with literature obtained at higher fields (13,29), at ULF we observe larger fractional reductions in T_1 than at higher field. Schneider et. al. (13) found that normative T_1 values at 3T in the thalamus and frontal white matter dropped 11% and 4% respectively between ~30 to 40 weeks gestation, whilst at 64mT the measured T_1 reduces in the deep grey matter and frontal white matter by 18% and 26% respectively.

Whilst this study performed T_1 mapping in-vivo, the paper by Koenig (18) presented values from unfixed samples excised from a 4 day old neonate who had died due to meconium aspiration. Ex-vivo samples from the cortical grey matter and subcortical white matter of the subject's left parietal lobe had T_1 values at 64mT of 494ms and 655ms, respectively. Whilst the grey matter

sample is consistent with our results (529-841ms), the white matter sample (taken at four days post-delivery) is considerably lower than our measurements at that age range (781-1292ms).

Future work will utilise the presented methodology to explore T_1 variation in more extremely premature infants, in addition to investigating the impact of mode of delivery, age of infant from birth, and pathology. Furthermore, we hope to use these methods to optimise T_1-weighted structural imaging in this population, as well as to validate measures of brain development that can be utilised wherever ULF-POC MRI can be deployed.

Acknowledgements

We thank Dr Nathan Artz for his input during the initial stages of this project. We also thank Christopher Bunton and Raminta Kniuraite for assistance with phantom construction. This work is supported by the Bill and Melinda Gates Foundation, the MRC (Translation Support Award: MR/V036874/1), and the Wellcome/EPSRC Centre for Medical Engineering [WT 203148/Z/16/Z]. PC is supported by a Medical Research Council Centre for Neurodevelopmental Disorders grant (MR/N026063/1). TA is supported by an MRC Clinician Scientist Fellowship [MR/P008712/1] and MRC translation support award [MR/V036874/1]. JOM is supported by a Sir Henry Dale Fellowship jointly funded by the Wellcome Trust and the Royal Society [Grant Number 206675/Z/17/Z].

Conflict of Interest Statement

Francesco Padormo was employed by Guy's & St Thomas' NHS Foundation Trust during experimental design, recruitment, all infant data collection, and prior to submission of the manuscript, but is now an employee of Hyperfine Inc. Lori Arlinghaus, John Pitts, Tianrui Luo and Dingtian Zhang are employed by Hyperfine Inc.

References

1. Turpin J, Unadkat P, Thomas J, et al. Portable Magnetic Resonance Imaging for ICU Patients. Crit. Care Explor. 2020;2:e0306 doi: 10.1097/CCE.0000000000000306.

2. Sheth KN, Mazurek MH, Yuen MM, et al. Assessment of Brain Injury Using Portable, Low-Field Magnetic Resonance Imaging at the Bedside of Critically Ill Patients. JAMA Neurol. 2021;78:41–47 doi: 10.1001/jamaneurol.2020.3263.

3. Mazurek MH, Cahn BA, Yuen MM, et al. Portable, bedside, low-field magnetic resonance imaging for evaluation of intracerebral hemorrhage. Nat. Commun. 2021;12:5119 doi: 10.1038/s41467-021-25441-6.

4. Marques JP, Simonis FFJ, Webb AG. Low-field MRI: An MR physics perspective. J. Magn. Reson. Imaging 2019;49:1528–1542 doi: 10.1002/jmri.26637.

5. Wald LL, McDaniel PC, Witzel T, Stockmann JP, Cooley CZ. Low-cost and portable MRI. J. Magn. Reson. Imaging 2020;52:686–696 doi: 10.1002/jmri.26942.

6. Holland BA, Haas DK, Norman D, Brant-Zawadzki M, Newton TH. MRI of normal brain maturation. Am. J. Neuroradiol. 1986;7:201–208.

7. Rutherford MA, Pennock JM, Murdoch-Eaton DM, Cowan FM, Dubowitz LM. Athetoid cerebral palsy with cysts in the putamen after hypoxic-ischaemic encephalopathy. Arch. Dis. Child. 1992;67:846–850 doi: 10.1136/adc.67.7_Spec_No.846.

8. Barkovich AJ, Kjos BO, Jackson DE, Norman D. Normal maturation of the neonatal and infant brain: MR imaging at 1.5 T. Radiology 1988;166:173–180 doi: 10.1148/radiology.166.1.3336675.

9. Zhai G, Lin W, Wilber KP, Gerig G, Gilmore JH. Comparisons of Regional White Matter Diffusion in Healthy Neonates and Adults Performed with a 3.0-T Head-only MR Imaging Unit. Radiology 2003;229:673–681 doi: 10.1148/radiol.2293021462.

10. Annink KV, van der Aa NE, Dudink J, et al. Introduction of Ultra-High-Field MR Imaging in Infants: Preparations and Feasibility. Am. J. Neuroradiol. 2020;41:1532–1537 doi: 10.3174/ajnr.A6702.

11. O'Reilly T, Teeuwisse WM, de Gans D, Koolstra K, Webb AG. In vivo 3D brain and extremity MRI at 50 mT using a permanent magnet Halbach array. Magn. Reson. Med. 2021;85:495–505 doi: 10.1002/mrm.28396.

12. Williams L-A, Gelman N, Picot PA, et al. Neonatal Brain: Regional Variability of in Vivo MR Imaging Relaxation Rates at 3.0 T—Initial Experience. Radiology 2005;235:595–603 doi: 10.1148/radiol.2352031769.

13. Schneider J, Kober T, Bickle Graz M, et al. Evolution of T1 Relaxation, ADC, and Fractional Anisotropy during Early Brain Maturation: A Serial Imaging Study on Preterm Infants. Am. J. Neuroradiol. 2016;37:155–162 doi: 10.3174/ajnr.A4510.

14. Kulikova S, Hertz-Pannier L, Dehaene-Lambertz G, Buzmakov A, Poupon C, Dubois J. Multi-parametric evaluation of the white matter maturation. Brain Struct. Funct. 2015;220:3657–3672 doi: 10.1007/s00429-014-0881-y.

15. Eminian S, Hajdu SD, Meuli RA, Maeder P, Hagmann P. Rapid high resolution T1 mapping as a marker of brain development: Normative ranges in key regions of interest Pouratian N, editor. PLOS ONE 2018;13:e0198250 doi: 10.1371/journal.pone.0198250.

16. Kühne F, Neumann W-J, Hofmann P, Marques J, Kaindl AM, Tietze A. Assessment of myelination in infants and young children by T1 relaxation time measurements using the magnetization-prepared 2 rapid acquisition gradient echoes sequence. Pediatr. Radiol. 2021;51:2058–2068 doi: 10.1007/s00247-021-05109-5.

17. Grotheer M, Rosenke M, Wu H, et al. White matter myelination during early infancy is linked to spatial gradients and myelin content at birth. Nat. Commun. 2022;13:997 doi: 10.1038/s41467-022-28326-4.

18. Koenig SH, Brown RD, Spiller M, Lundbom N. Relaxometry of brain: Why white matter appears bright in MRI. Magn. Reson. Med. 1990;14:482–495 doi: https://doi.org/10.1002/mrm.1910140306.

19. Rearick T, Charvat GL, Rosen MS, Rothberg JM. Noise suppression methods and apparatus. 2017.

20. Yarnykh VL. Actual flip-angle imaging in the pulsed steady state: A method for rapid three-dimensional mapping of the transmitted radiofrequency field. Magn. Reson. Med. 2007;57:192–200 doi: 10.1002/mrm.21120.

21. Smith SM. Fast robust automated brain extraction. Hum. Brain Mapp. 2002;17:143–155 doi: 10.1002/hbm.10062.

22. Gudbjartsson H, Patz S. The rician distribution of noisy mri data. Magn. Reson. Med. 1995;34:910–914 doi: 10.1002/mrm.1910340618.

23. Karlsen OT, Verhagen R, Bovée WMMJ. Parameter estimation from Rician-distributed data sets using a maximum likelihood estimator: Application to t1 and perfusion measurements. Magn. Reson. Med. 1999;41:614–623 doi: 10.1002/(SICI)1522-2594(199903)41:3<614::AID-MRM26>3.0.CO;2-1.

24. Jenkinson M, Smith S. A global optimisation method for robust affine registration of brain images. Med. Image Anal. 2001;5:143–156 doi: 10.1016/S1361-8415(01)00036-6.

25. Jenkinson M, Bannister P, Brady M, Smith S. Improved Optimization for the Robust and Accurate Linear Registration and Motion Correction of Brain Images. NeuroImage 2002;17:825–841 doi: 10.1006/nimg.2002.1132.

26. O'Reilly T, Webb AG. In vivo T1 and T2 relaxation time maps of brain tissue, skeletal muscle, and lipid measured in healthy volunteers at 50 mT. Magn. Reson. Med. 2022;87:884–895 doi: 10.1002/mrm.29009.

27. Ma D, Gulani V, Seiberlich N, et al. Magnetic resonance fingerprinting. Nature 2013;495:187–192.

28. Leitão D, Teixeira RPAG, Price A, Uus A, Hajnal JV, Malik SJ. Efficiency analysis for quantitative MRI of T1 and T2 relaxometry methods. Phys. Med. Ampmathsemicolon Biol. 2021;66:15NT02 doi: 10.1088/1361-6560/ac101f.

29. Maitre NL, Slaughter JC, Stark AR, Aschner JL, Anderson AW. Validation of a brain MRI relaxometry protocol to measure effects of preterm birth at a flexible postnatal age. BMC Pediatr. 2014;14:84 doi: 10.1186/1471-2431-14-84.

Figure Legends

Figure 1 - Pulse sequence diagram of inversion recovery 3D turbo spin echo. The sequence is comprised of an adiabatic inversion pulse, a turbo spin echo read-out train, and a centre frequency navigator.

Figure 2 – Results of contrast phantom validation experiment.

Figure 3 – Results of homogeneity phantom validation experiment.

Figure 4 – Three slices from a single neonate (gestation 33+2, post-menstrual age 34+0) A) Source images for each T1w acquisition; B,C) M0 and T1 maps; and D-F) Raw datapoints (blue dots) and predicted signals (red lines/cross) based on measured T1 and M0. The blue datapoint/red cross

away from the curve corresponds to the TR=3000ms datapoint, and therefore belongs to a separate inversion-recovery curve.

Figure 5 – The effect of motion correction on T1 maps of a neonate born at 38+3 gestation and imaged at 41+0 post-menstrual age. Coronal (A) and axial (B) T1 maps for three iterations of the reconstruction pipeline. Coronal (C) and axial (D) the relative root-mean square error maps between the input images and predicted output images at each iteration.

Figure 6 – T1 maps of eight subjects over the full age range of neonates scanned in this study.

Figure 7 – T1 versus postmenstrual age. The colour of each datapoint indicates the acquisition protocol from Table I.

Table I – Imaging parameters of the protocols used within presented study, and number of acquisitions each protocol was utilised for.

Supporting Information Video S1 – Top row: coronal images prior to motion compensation. Contrast changes across the volume are seen due to varying sequence parameters, and inter-image motion is observed. Bottom row: After inter-volume motion compensation, the brain remains static in the frame. Nonlinear motion is still observed outside of the head, but is not relevant for T_1 mapping in the brain.

Supporting Information Video S2 – Top row: saggital images prior to motion compensation. Contrast changes across the volume are seen due to varying sequence parameters, and inter-image motion is observed. Bottom row: After inter-volume motion compensation, the brain remains static in the frame. Nonlinear motion is still observed outside of the head, but is not relevant for T_1 mapping in the brain.